Journal of Molecular Catalysis A: Chemical 307 (2009) 105–114

Contents lists available at ScienceDirect

Journal of Molecular Catalysis A: Chemical

journal homepage: www.elsevier.com/locate/molcata

Ni-B amorphous alloy deposited on an aminopropyl and methyl co-functionalized SBA-15 as a highly active catalyst for chloronitrobenzene hydrogenation

Hui Li, Ye Xu, Haixia Yang, Fang Zhang, Hexing Li*

Department of Chemistry, Shanghai Normal University, Shanghai 200234, PR China

ARTICLE INFO

Article history:
Received 24 November 2008
Received in revised form 8 March 2009
Accepted 9 March 2009
Available online 21 March 2009

Keywords:
Ni-B amorphous alloy catalyst
Mesoporous silica
Co-functionalization
p-Chloronitrobenzene hydrogenation to *p*-chloroaniline

ABSTRACT

The synthesis and characterization of SBA-15 type mesoporous silica containing surfaces functionalized with aminopropyl and methyl groups (NH_2&CH_3-SBA-15) were reported. The Ni-B amorphous alloy deposited on such support showed higher activity and selectivity in liquid-phase hydrogenation of *p*-chloronitrobenzene (*p*-CNB) to *p*-chloroaniline (*p*-CAN) owing to the synergetic promotions from both the aminopropyl and methyl groups. The aminopropyl could greatly enhance the dispersion of Ni-B alloy particles via coordination with Ni^{2+} ions, leading to high activity. While, the methyl could enhance the surface hydrophobicity which facilitated the desorption of the target product *p*-CAN and thus inhibited its further dechlorination. Besides, the strong hydrophobicity also enhanced the B-content in the Ni-B alloys, which favored the activation and hydrogenation of the NO_2-group in *p*-CNB molecule, leading to high selectivity. This work clearly reveals the importance of organization of different functional groups on the surface of heterogeneous catalysts.

1. Introduction

Amorphous alloys have proven powerful metal catalysts owing to their unique long-range disordering while short-range ordering structure [1–3], among which Ni-B amorphous alloy is one of the most thoroughly investigated catalysts. To increase the active surface area and improve the thermal stability, supported Ni-B catalysts have been synthesized through impregnation-reductant method [4–7]. Because of high surface areas, ordered pore channel, and uniformity in pore size, highly ordered mesoporous materials can act as promising carriers for depositing Ni-B amorphous alloy nanoparticles [8–11]. However, it is found that the supported Ni-B catalyst by using pure mesoporous silica usually exhibit nonuniform distribution of Ni-B particles and even blockage of the pore entrance, which eventually limits the activity and especially, the selectivity [8].

Organic–inorganic hybrid materials represent a new class of materials [12–16]. Incorporation of multifunctional groups into the channel of ordered mesoporous materials allows for molecular-level fine-tuning of catalytic performances [17–19]. Moreover, the surface hydrophilic–hydrophobic properties of the ordered mesoporous materials can be modified through immobilization of organic groups, which is essential in order to optimize the catalysis for some structure-sensitive reactions [20]. For example, one reaction requiring heterogeneous catalysts with proper surface properties is the liquid-phase hydrogenation of *p*-chloronitrobenzene (*p*-CNB) to *p*-chloroaniline (*p*-CAN). This reaction is of industrial importance in manufacturing dyes, drugs, herbicides, pesticides, and other fine chemicals, and is always catalyzed by metal catalysts [21]. Increasing the surface hydrophobic property of catalysts can enhance *p*-CAN selectivity, since *p*-CAN is a polar molecule that is easily desorbed from the hydrophobic catalyst surface and the side reactions such as dechlorination are therefore suppressed [22]. Recently, we had demonstrated that Ni-based catalysts, including Ni-based amorphous alloys, were suitable catalysts for *p*-CNB hydrogenation [23–25]. More interestingly, the surface composition of Ni-based amorphous alloys, especially the boron content, could be adjusted based on the preparation method, which had significant effect on the catalytic properties [23,24]. However, the preparation of Ni-B amorphous alloy supported on organic–inorganic hybrid materials and the effects of organic groups on their composition and thus, their catalytic performances, had never addressed so far.

Herein, we report a novel Ni-B amorphous alloy catalyst supported on aminopropyl and methyl co-functionalized silica with ordered mesoporous structure similar to SBA-15, which is synthesized by co-condensation of tetraethoxysilane (TEOS) and organosilanes containing aminopropyl and methyl groups in the presence of P123 template. This catalyst exhibits high activity and selectivity during liquid-phase hydrogenation of *p*-CNB to *p*-CAN. The synergetic promoting effects from both the aminopropyl and the methyl functionalities are well established.

* Corresponding author. Tel.: +86 21 64322272; fax: +86 21 64322272.
E-mail address: hexing-li@shnu.edu.cn (H. Li).

1381-1169/$ – see front matter © 2009 Elsevier B.V. All rights reserved.
doi:10.1016/j.molcata.2009.03.015

2. Experimental

2.1. Catalyst preparation

Pure SBA-15 silica was synthesized according to the method reported by Zhao et al. [26]. In a typical run of syntheses, 2.0 g P123 surfactant was dissolved at 313 K in a solution comprised of 15 mL water and 60 mL 2 M HCl, followed by adding 4.5 mL TEOS. After being stirred at 313 K for 24 h and aged at 373 K for another 24 h, the solid product was thoroughly washed with water, followed by drying in vacuum at 353 K for 8 h. The surfactant and other organic residues were extracted by refluxing the sample in ethanol (EtOH) at 353 K for 24 h. The SBA-15 sample was finally obtained after being dried at 353 K under vacuum for 8 h.

Functionalized SBA-15 samples were synthesized through P123 directed co-condensation of TEOS with aminopropyl triethoxysilane (APTES) and/or methyl triethoxysilane (MTES) in an acid solution, during which TEOS was pre-hydrolyzed at 313 K for 3 h [27]. Other procedures are the same as those for preparing SBA-15. The as-prepared samples were denoted as NH_2-SBA-15, CH_3-SBA-15 and NH_2&CH_3-SBA-15. In most cases, the molar ratios of methyl and aminopropyl to total silicon in the mother mixture were fixed at 7.1%.

The supported Ni-B samples were prepared according to the following procedure. 1.0 g of a support was impregnated by 3.0 mL 0.85 M $NiCl_2$ aqueous solution overnight. After being dried under microwave irradiation at 393 K for 35 min, 5.0 mL 2.0 M KBH_4 aqueous solution was added dropwise at 273 K and was stirred continuously until no bubbles released. The solid was washed free from Cl^- or K^+ ions with water until a pH ~ 7 was achieved, followed by three washing with EtOH, and finally soaked in EtOH until use.

2.2. Characterization

The composition of catalysts was analyzed by means of inductively coupled plasma (ICP; Jarrell-Ash Scan 2000). N_2 adsorption isotherms were measured at 77 K on a Quantachrome NOVA 4000e apparatus. Based on the desorption branches, the surface area (S_{BET}), the pore size distribution, the average pore size (D_P), and the pore volume (V_P) were calculated by using Barrett–Joyner–Halenda (BJH) model. Transmission electron microscopy (TEM) images and selected area electron diffraction (SAED) patterns were obtained on a JEOL JEM-2010 electron microscope, operated at an acceleration voltage of 200 kV. Solid-state NMR spectra were obtained on a Bruker AV-400 NMR spectrometer. Fourier transform infrared (FTIR) spectra were recorded on a Nicolet Magna 550 spectrometer by KBr technique. Thermogravimetric analysis (TGA) was carried out on a Du Pont 951 thermogravimetric analyzer with a ramping rate of 10 K/min in 50 mL/min of air flow. Low-angle and high-angle X-ray diffraction (XRD) patterns were collected on a Rigaku Dmax-3C diffractometer with Cu Kα radiation. X-ray photoelectron spectroscopy (XPS) measurements were performed on a Perkin-Elmer PHI 5000C ESCA system. All the binding energies were calibrated by using the contaminant carbon (C 1s = 284.6 eV) as a reference. When conducting the XPS experiment, the sample soaked in ethanol solution was mounted on the sample plate. After removing solvents in Ar flow, the sample was degassed in the pretreatment chamber under 1×10^{-6} Torr for 4 h and then transferred to the analyzing chamber by means of probe insertion. All the pretreatments and XPS characterization were carried out in the Ar atmosphere so that, the oxidation of surface Ni can be avoided. Hydrogen chemisorption were conducted on a Quantachrome CHEMBET 3000 instrument, from which the active surface area (S_{act}) was calculated assuming H/Ni(s) = 1 and a surface area per Ni atom = 6.5×10^{-20} m^2 [28].

2.3. Activity test

Liquid-phase hydrogenation of *p*-CNB was performed at 1.0 MPa H_2 and 373 K in a 200 mL stainless steel autoclave containing 1.0 g catalyst, 20 mmol of *p*-CNB, and 60 mL EtOH. The reaction system was stirred vigorously (1000 rpm) to eliminate the diffusion effect. The reaction mixture was sampled at equal intervals for product analysis on a gas chromatograph (GC 9800) equipped with a flame ionization detector (FID) and an AC-5 column using *n*-$C_{12}H_{25}OH$ as internal standard, from which both the conversion and the selectivity were calculated. Reproducibility was checked by repeating the runs at least three times and was found to be within acceptable limits (±5%). Supports alone did not show any catalytic activity.

3. Results and discussion

3.1. Structural characteristics

The XPS spectra (Fig. 1) demonstrated that all the Ni species were present in metallic state with the binding energy (BE) around 853.0 eV in the Ni $2p_{3/2}$ level [29]. However, the B-species were present in the elemental B and the oxidized B, corresponding to the BE around 188.2 and 192.3 eV in B 1s level, respectively. The BE of the elemental B was 1.1 eV higher than that of pure B (187.1 eV) [30], suggesting that the elemental B was not present in free state but alloyed with the metallic Ni, in which partial electrons transferred from B to Ni, though no significant BE shift of Ni was observed due to its bigger atomic size [30]. The XRD patterns (Fig. 2) demonstrated that, besides a broad peak around $2\theta = 22^\circ$ corresponding to amorphous SiO_2 [31], all the Ni-B samples displayed only one broad peak around $2\theta = 45^\circ$ indicative of the typical amorphous structure [32]. The combined results from both the XRD and the aforementioned XPS demonstrated that all the samples were present in Ni-B amorphous alloys. Calcination of these samples at 873 K for 2 h in N_2 flow resulted in various diffraction peaks corresponding to metallic Ni and crystalline Ni-B alloy appeared, implying the occurrence of crystallization process, together with partial decomposition of the Ni-B alloy into metal Ni.

The FTIR spectra in Fig. 3 revealed that the pure SBA-15 displayed a broad absorbance band between 3600 and 3200 cm^{-1}, corresponding to the stretching vibration of the O–H bonds in the surface silanol groups and the adsorbed water molecules. The absorbance band at 1635 cm^{-1} was assigned to the deformational vibrations

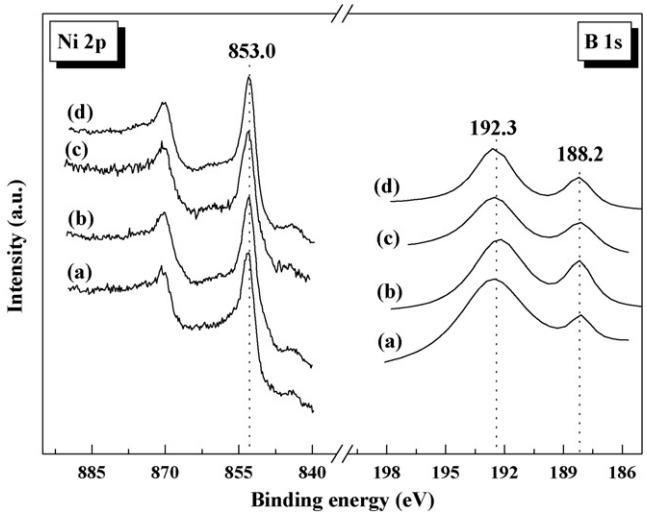

Fig. 1. XPS spectra of (a) Ni-B/SBA-15, (b) Ni-B/NH_2-SBA-15, (c) Ni-B/CH_3-SBA-15, and (d) Ni-B/NH_2&CH_3-SBA-15.

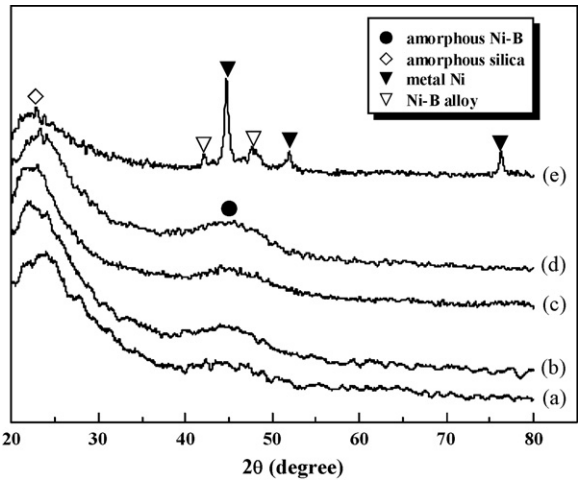

Fig. 2. Wide-angle XRD patterns of (a) Ni-B/SBA-15, (b) Ni-B/NH_2-SBA-15, (c) Ni-B/CH_3-SBA-15, (d) Ni-B/NH_2&CH_3-SBA-15, and (e) Ni-B/NH_2&CH_3-SBA-15 treated at 873 K for 2 h in N_2 flow.

from adsorbed water molecules [33]. While, the absorbance bands around 960 and 1100 cm^{-1} could be attributed to the Si–O stretching vibration from silanol groups and the Si–O–Si vibration of siloxane, respectively. Besides these absorbance bands, all the R-SBA-15 samples (R = NH_2- and/or CH_3-groups) displayed additional absorbance bands at 2926, 2847, 1463 and 722 cm^{-1} indicative of asymmetric stretching, symmetric stretching, bending vibrations of aliphatic C–H bonds [34] and the vibration of Si–C bonds [35]. In addition, both the NH_2-SBA-15 and the NH_2&CH_3-SBA-15 displayed absorbance band at 1521 cm^{-1} characteristic of N–H bending vibration. All of these results demonstrated the successful incorporation of aminopropyl and methyl groups into the silica network, which could be further confirmed by the solid-state NMR spectra. As shown in Fig. 4, the ^{29}Si CP MAS NMR spectra displayed three up-field resonance peaks for the siloxane corresponding to Q^4 ($\delta = -111$ ppm), Q^3 ($\delta = -103$ ppm), Q^2 ($\delta = -93$ ppm), where $Q^n = Si(OSi)_n(OH)_{4-n}$ ($n = 2$–4). Two down-field organosilane signals were observed at −66 and −55 ppm, corresponding to T^3 and T^2, where $T^m = RSi(OSi)_m(OH)_{3-m}$ ($m = 1$–3), which confirmed the incorporation of the organic groups into the silica framework via forming C–Si bond [36]. In comparison with the pure SBA-15, all the R-SBA-15 samples showed lower signal intensities of Q^3/Q^4 due

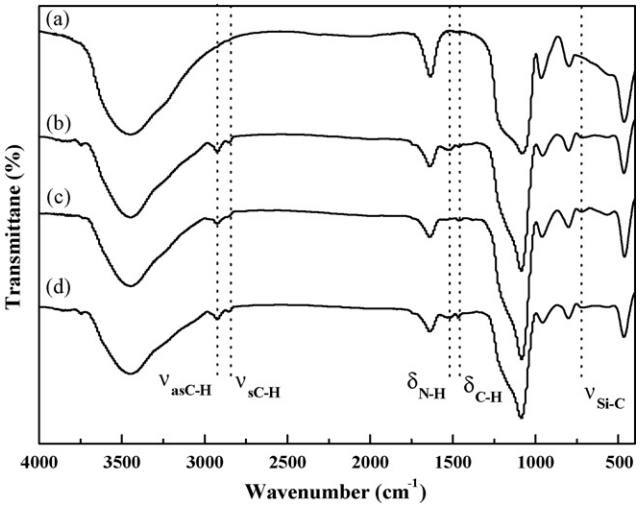

Fig. 3. FTIR spectra of (a) SBA-15, (b) NH_2-SBA-15, (c) CH_3-SBA-15, and (d) NH_2&CH_3-SBA-15.

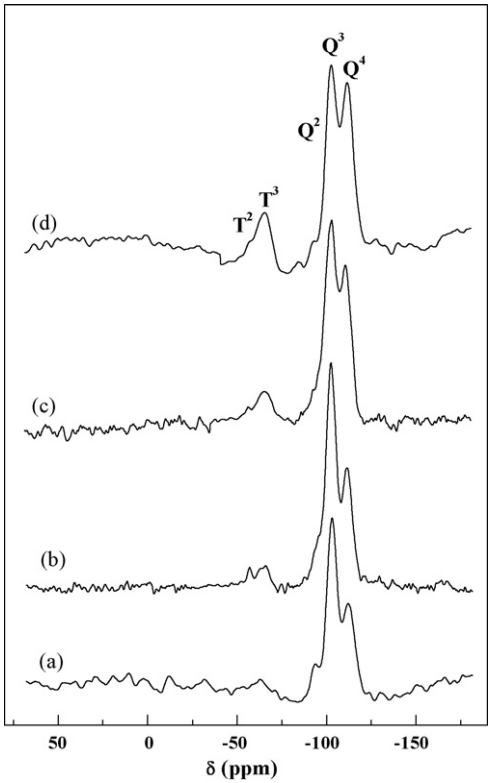

Fig. 4. ^{29}Si MAS NMR spectra of (a) SBA-15, (b) NH_2-SBA-15, (c) CH_3-SBA-15, and (d) NH_2&CH_3-SBA-15.

to the substitution of Si–O bonds by Si–C bonds. The $T^m/(T^m + Q^n)$ ratios were determined as 7.5%, 7.3%, and 14.8% in the NH_2-SBA-15, CH_3-SBA-15 and the NH_2&CH_3-SBA-15 samples, respectively, which were almost the same as the contents of organic groups in initial mixture, suggesting that the organosilicane completely co-condensed with the TEOS, i.e., the loss of organic groups during the co-condensation process could be neglected. The TGA curves (Fig. 5) demonstrated that the decomposition of organic groups anchored on SBA-15 occurred between 463 and 873 K. The NH_2&CH_3-SBA-15 and Ni-B/NH_2&CH_3-SBA-15 samples exhibited weight loss of organic groups about 20% and 17%, respectively. Taking into account that the Ni loading in Ni-B/NH_2&CH_3-SBA-15 is 12 wt%, a rough estimation gave a weight loss in Ni-B/NH_2&CH_3-SBA-15 should be 18%. These results indicated no significant leaching of organic groups during impregnation with Ni^{2+} ions, pretreatment under microwave and the subsequent reduction with BH_4^-.

As shown in Fig. 6, all the R-SBA-15 and the Ni-B/R-SBA-15 samples with different contents of NH_2- and/or CH_3-groups (see Table 1) displayed well-defined type-IV N_2 adsorption–desorption isotherms with H_1 hysteresis loop characteristic of two-dimensional hexagonal mesoporous structure. By applying the BJH method to the desorption branches, narrow pore size distributions were obtained (see the attached).

Meanwhile, the low-angle XRD patterns (Fig. 7) revealed that the pure SBA-15, the functionalized SBA-15 and the supported Ni-B samples displayed an intense (1 0 0) diffraction peak around $2\theta = 0.77^\circ$ and two weak peaks at $2\theta = 1.4$ and 1.6° indicative of (1 1 0) and (2 0 0) diffractions, which are characteristic of the 2D hexagonal (*P6mm*) structure [26]. Functionalization with organic groups and deposition with Ni-B nanoparticles caused significant decrease in the intensity of the (1 0 0) diffraction peaks and even the disappearance of the (1 1 0) and (2 0 0) diffraction peaks, implying the reduced ordering degree of the mesoporous structure which could be mainly attributed to the occupation of organic groups and

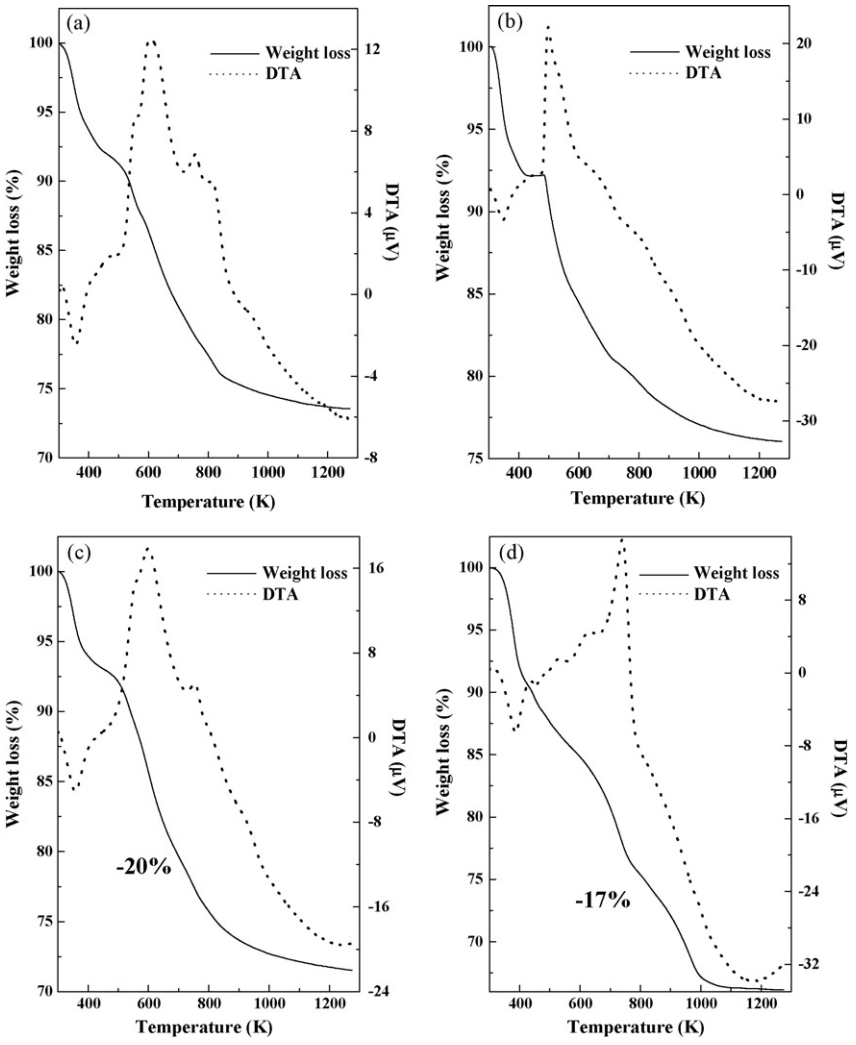

Fig. 5. TGA and DTA curves of (a) NH_2-SBA-15, (b) CH_3-SBA-15, (c) NH_2&CH_3-SBA-15, and (d) Ni-B/NH_2&CH_3-SBA-15.

Ni-B nanoparticles in the pore channels. A marked shift of the (1 0 0) diffraction peak towards larger 2θ angles demonstrated a shrinkage of the cell dimension of the resulting mesostructured materials.

Fig. 8 shows the TEM morphologies and SAED images (the inset) of the R-SBA-15 and the Ni-B/R-SBA-15 samples. From SAED images, one could see that all the Ni-B/R-SBA-15 samples displayed successive diffraction halos indicative of typical amorphous alloy structure [37], in agreement with the above XRD characterizations. Meanwhile, the TEM images demonstrated the ordered mesoporous structure. In the Ni-B/SBA-15 sample, most of Ni-B nanoparticles were deposited on the outer surface, the Ni-B nanoparticles in Ni-B/NH_2-SBA-15 were uniformly distributed in

Table 1
Physical characteristics of various silicas and supported catalysts[a].

Sample	C_{NH_2} (%)	C_{CH_3} (%)	d_{100} (nm)	a (nm)	S_{BET} ($m^2\,g^{-1}$)	V_P ($cm^3\,g^{-1}$)	D_P (nm)	C_{BET}
SBA-15	0	0	11.5	13.3	777	1.3	8.0	140
Ni-B/SBA-15	0	0	10.9	12.5	684	1.2	7.1	129
NH_2-SBA-15(a)	4.5	0	11.3	13.0	589	0.8	6.5	94
NH_2-SBA-15	7.1	0	11.1	12.8	550	0.7	5.3	86
NH_2-SBA-15(b)	9.1	0	10.9	12.5	535	0.6	4.8	70
NH_2-SBA-15(c)	14	0	10.7	12.3	499	0.3	3.5	64
Ni-B/NH_2-SBA-15	7.1	0	11.0	12.7	501	0.6	3.7	76
CH_3-SBA-15(a)	0	4.5	10.5	12.1	685	1.0	6.4	77
CH_3-SBA-15	0	7.1	10.4	12.0	586	0.8	5.6	70
CH_3-SBA-15(b)	0	9.1	10.4	12.0	484	0.7	4.4	56
CH_3-SBA-15(c)	0	14	10.2	11.7	462	0.6	4.1	34
Ni-B/CH_3-SBA-15	0	7.1	10.4	12.0	524	0.5	3.8	65
NH_2&CH_3-SBA-15(a)	4.5	4.5	10.7	12.3	583	0.8	5.0	59
NH_2&CH_3-SBA-15	7.1	7.1	10.5	12.1	571	0.7	4.4	53
NH_2&CH_3-SBA-15(b)	9.1	9.1	10.1	11.6	521	0.6	4.2	50
Ni-B/NH_2&CH_3-SBA-15	7.1	7.1	10.1	11.6	523	0.5	3.8	51

[a] C_{NH_2} and C_{CH_3} refer to the molar ratios of NH_2/Si and CH_3/Si, respectively. $a = 2d_{100}/\sqrt{3}$.

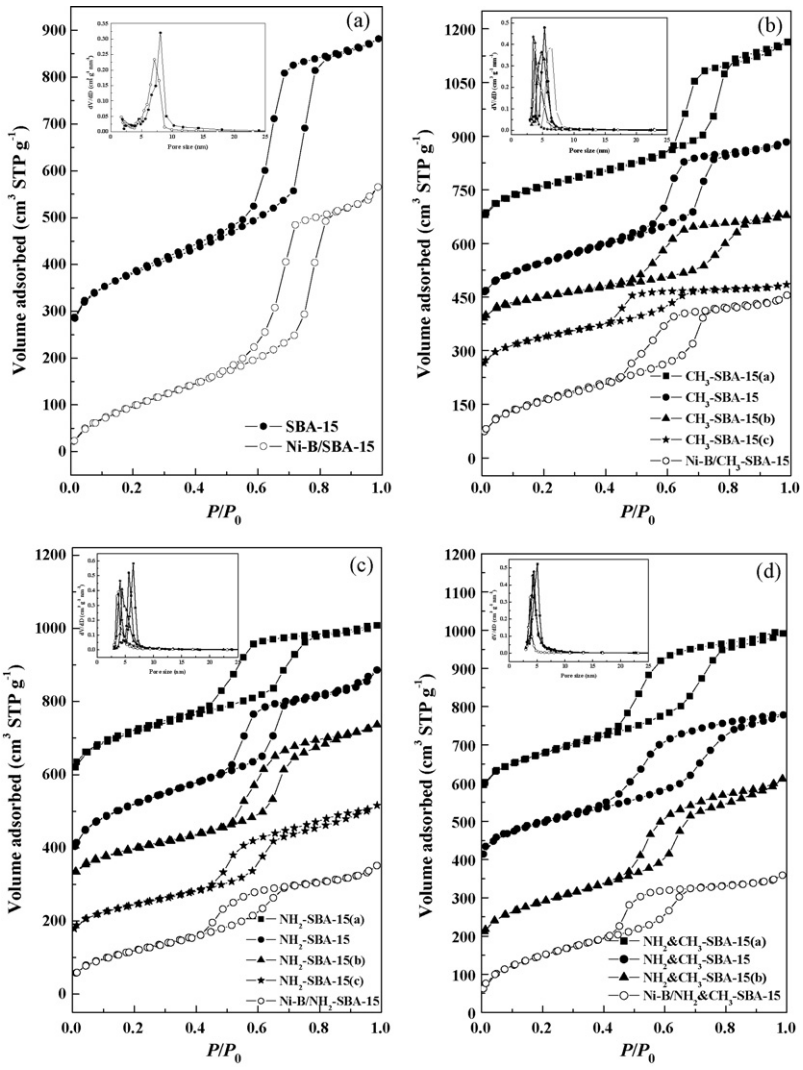

Fig. 6. N_2 adsorption–desorption isotherms and pore size distributions (inset) of (a) SBA-15 and Ni-B/SBA-15, (b) CH_3-SBA-15(x) and Ni-B/CH_3-SBA-15(x), (c) NH_2-SBA-15(x) and Ni-B/NH_2-SBA-15(x), and (d) NH_2&CH_3-SBA-15(x) and Ni-B/NH_2&CH_3-SBA-15.

the mesoporous channels with much smaller size. This could be attributed to the coordination of the Ni^{2+} ions with the NH_2-groups originally incorporated into the pore channels of SBA-15. Reduction of these coordinated Ni^{2+} ions with BH_4^- led to the Ni-B nanoparticles located inside the mesoporous channels. The uniform particle size could be attributed to the smooth reduction between the coordinated Ni^{2+} ions and BH_4^- in comparison with the direct reduction between free Ni^{2+} ions and BH_4^-, which might diminish the particle agglomeration taking into account that the reduction is strongly exothermic. Meanwhile, the pore channels also confined the particle growth and gathering. The presence of CH_3-groups could also improve the particle distribution owing to the dispersing effect of the hydrophobic groups [38].

Based on the desorption branches of N_2 sorption isotherms, some structural parameters were calculated and listed in Table 1. The decreases in the d_{100} spacing and in the lattice parameter ($a = 2d_{100}/\sqrt{3}$) with the enhanced contents of organic groups could be explained by the perturbation of the self-assembly of the silica precursor caused by APTES and/or MTES [39]. The incorporation of the organic groups into SBA-15 caused significant decrease in the S_{BET}, V_P and D_P, which could be mainly attributed to the increase of the wall thickness due to the coverage of the wall surface with these organic groups. The supported Ni-B samples exhibited even lower S_{BET}, V_P and D_P values, obviously due to the occupation of the Ni-B nanoparticles on pore surface and in pore channels. Meanwhile, the BET constant (C_{BET}) value of CH_3-SBA-15 and NH_2-SBA-15 samples was much lower than the pure SBA-15, showing that the functionalization of SBA-15 with organic groups led to enhanced hydrophobicity [40]. The functionalization with MTES (CH_3) displayed higher surface hydrophobicity than the functionalization with APTES (NH_2–CH_2–CH_2–CH_2), which could be understood by considering the hydrophilicity of the NH_2 terminal. The NH_2&CH_3-SBA-15 exhibited higher surface hydrophobicity than either the NH_2-SBA-15 or the CH_3-SBA-15 with the same contents of NH_2- or CH_3-groups owing to the synergetic effects from the co-functionalization.

The Ni loadings on the support and the bulk compositions of the Ni-B amorphous alloys were determined by ICP analysis, which revealed that all the supported catalysts possessed the similar Ni loading around 12 wt% and the similar bulk composition regardless of the surface functionalization with organic groups. The surface compositions of the Ni-B amorphous alloys were calculated according to XPS spectra by using 0.13 and 2.50 as the PHI sensitivity factors to B 1s and Ni $2p_{3/2}$ [30]. As shown in Table 2, the surface composition data demonstrated that the Ni-B amorphous alloys deposited on the R-SBA-15 supports are slightly surface enriched with B-species. On one hand, the B-enrichment could be attributed to the enhanced surface hydrophobicity, which could

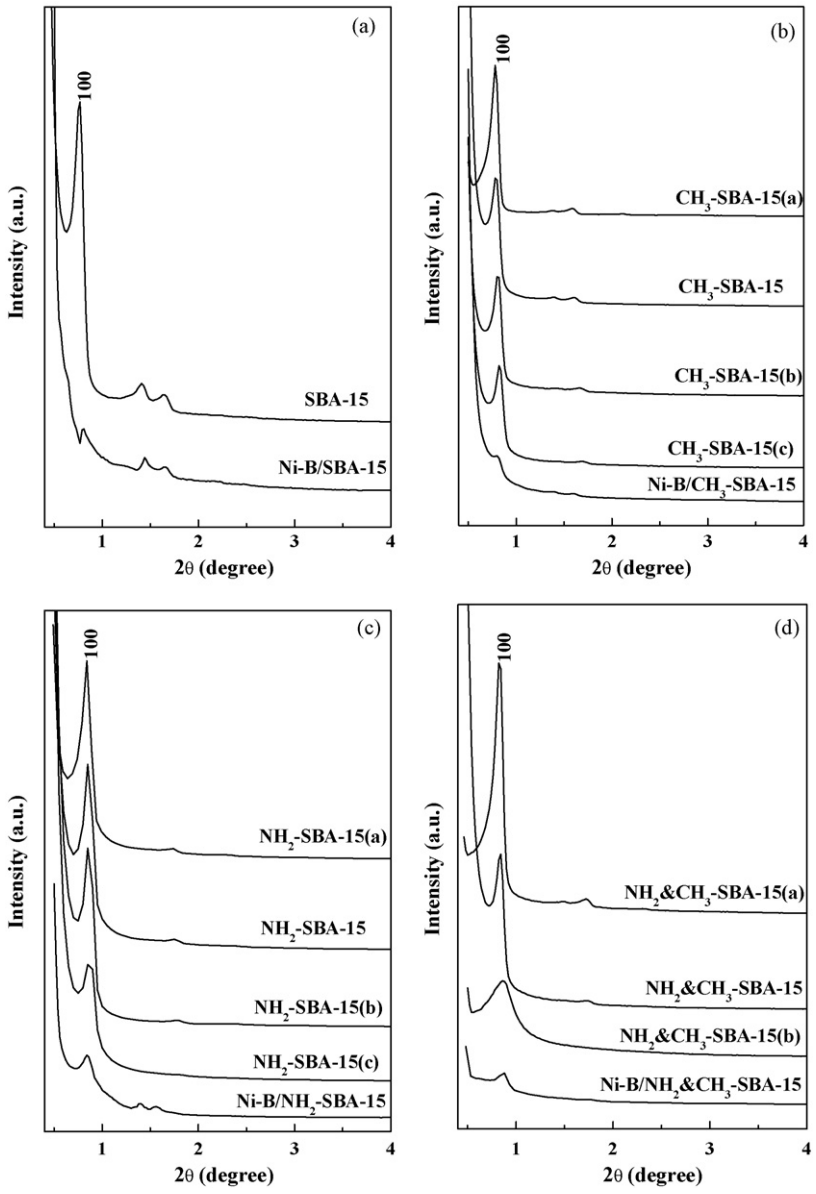

Fig. 7. Low-angle XRD patterns of (a) SBA-15 and Ni-B/SBA-15, (b) CH_3-SBA-15(x) and Ni-B/CH_3-SBA-15(x), (c) NH_2-SBA-15(x) and Ni-B/NH_2-SBA-15(x), and (d) NH_2&CH_3-SBA-15(x) and Ni-B/NH_2&CH_3-SBA-15.

Table 2
Structural and catalytic properties of different Ni-B catalysts[a].

Catalyst	Surf. composition (atomic ratio)	S_{Ni} ($m^2\ g^{-1}$)	TOF[b] (s^{-1})	$Yield_{max}$[c] (%) (reaction time, min)
Ni-B/SBA-15	$Ni_{83}B_{17}$	15	0.015	80 (390)
Ni-B/NH_2-SBA-15(a)	$Ni_{78}B_{22}$	19	0.031	85 (180)
Ni-B/NH_2-SBA-15	$Ni_{75}B_{25}$	20	0.039	87 (120)
Ni-B/NH_2-SBA-15(b)	$Ni_{75}B_{25}$	25	0.038	77 (100)
Ni-B/NH_2-SBA-15(c)	$Ni_{74}B_{26}$	28	0.039	68 (80)
Ni-B/CH_3-SBA-15(a)	$Ni_{81}B_{19}$	16	0.018	82 (360)
Ni-B/CH_3-SBA-15	$Ni_{80}B_{20}$	16	0.026	88 (240)
Ni-B/CH_3-SBA-15(b)	$Ni_{80}B_{20}$	18	0.025	88 (240)
Ni-B/CH_3-SBA-15(c)	$Ni_{79}B_{21}$	18	0.026	89 (225)
Ni-B/NH_2&CH_3-SBA-15(a)	$Ni_{80}B_{20}$	18	0.024	89 (255)
Ni-B/NH_2&CH_3-SBA-15	$Ni_{75}B_{25}$	19	0.040	90 (120)
Ni-B/NH_2&CH_3-SBA-15(b)	$Ni_{75}B_{25}$	21	0.038	84 (120)

[a] Reaction conditions: 1.0 g of catalyst, 20 mmol of *p*-CNB, 60 mL of EtOH, T = 353 K, P_{H_2} = 1.0 MPa, and stirring rate = 1000 rpm.
[b] TOF is expressed as the number of *p*-CNB molecule converted per second on per surface Ni site.
[c] The maximum yield of the target product *p*-CAN and the time needed to reach the maximum yield.

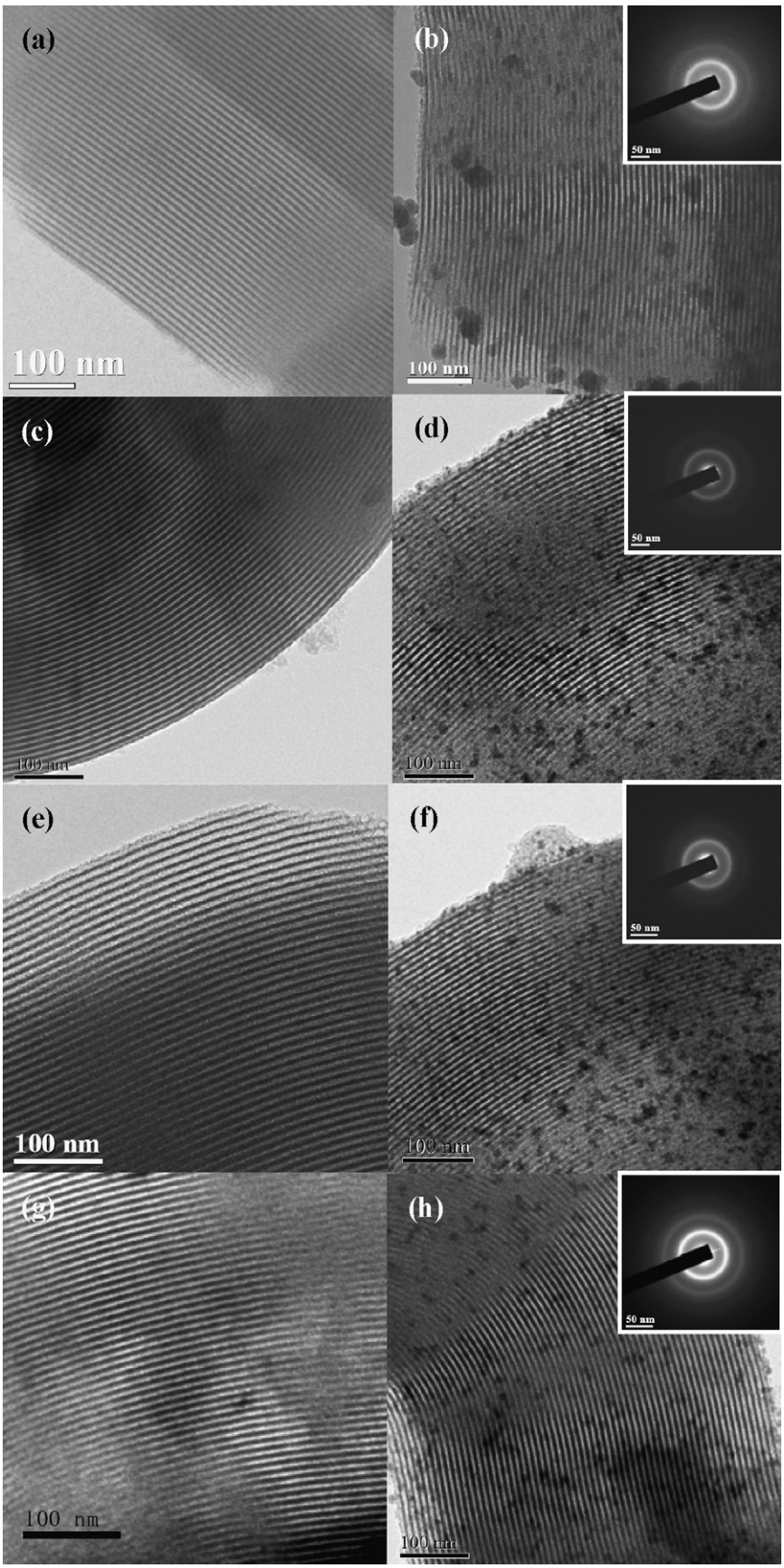

Fig. 8. TEM images of (a) SBA-15, (b) Ni-B/SBA-15, (c) NH_2-SBA-15, (d) Ni-B/NH_2-SBA-15, (e) CH_3-SBA-15, (f) Ni-B/CH_3-SBA-15, (g) NH_2&CH_3-SBA-15, and (h) Ni-B/NH_2&CH_3-SBA-15. Insets are the SAED patterns of the Ni-B particles.

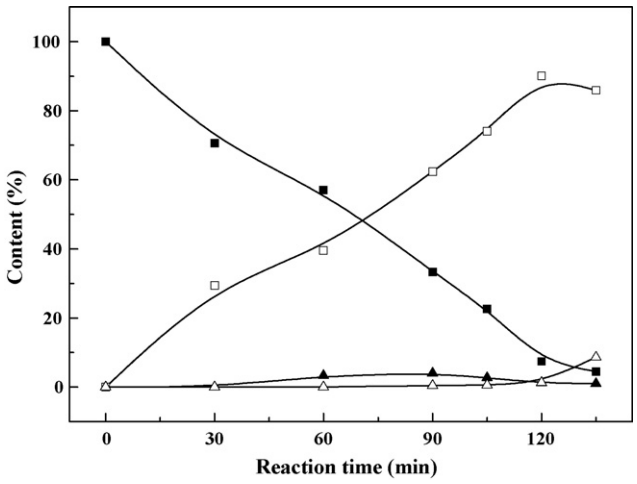

Fig. 9. Hydrogenation of *p*-CNB over Ni-B/NH_2&CH_3-SBA-15 amorphous alloy catalyst as a function of reaction time. (■) *p*-CNB, (□) *p*-CAN, (▲) NB, and (△) AN. Reaction conditions are listed in Table 2.

slow down the reaction rate between Ni^{2+} and BH_4^-. Taking into account that the reduction of Ni^{2+} by BH_4^- is strongly exothermic, the smooth reaction could effectively inhibit the breakage of Ni-B bonds, leading to the higher B-content in the Ni-B alloy [41]. The NH_2-functionalization could further enhance the B-content in the Ni-B alloy owing to the coordination of NH_2-ligands with Ni^{2+}, making the reaction between Ni^{2+} and BH_4^- proceeded even more smoothly [42]. The smooth reaction could also account for the higher S_{Ni} values of the Ni-B/R-SBA-15 amorphous catalysts than that of the Ni-B/SBA-15. Meanwhile, the increase of S_{Ni} with the enhanced contents of organic groups on the SBA-15 support could also be explained in this way.

3.2. Catalytic behaviors

Fig. 9 shows the reaction profile of *p*-CNB hydrogenation over Ni-B/NH_2&CH_3-SBA-15. Besides the main product (*p*-CAN), only aniline (AN) and nitrobenzene (NB) were identified as byproducts under the present conditions, which were also observed over other catalysts, suggesting that the *p*-CNB hydrogenation possibly followed the pathways described in Scheme 1. As shown in Fig. 10, the *p*-CNB conversion increased almost linearly with the reaction time over Ni-B amorphous alloy catalysts supported on pure SBA-15, NH_2-SBA-15, CH_3-SBA-15, and NH_2&CH_3-SBA-15, implying that the *p*-CNB hydrogenation was zero-order with respect to *p*-CNB concentration. Based on the reaction profiles, the catalytic parameters (TOF, the maximum yield of the target product and the corresponding reaction time) of different catalysts were calculated. From the data in Table 2 and the conversion–time curves in Fig. 10, the following conclusions were drawn:

1. All the Ni-B/R-SBA-15 catalysts exhibited much higher activity than Ni-B/SBA-15 and activity increased with the enhanced contents of R-groups incorporated in the SBA-15 support, showing the promotional effect of surface functionalization with organic groups. This could be mainly attributed to the enhanced surface hydrophobicity, which could improve the dispersion of Ni-B nanoparticles, leading to higher metallic surface (S_{Ni}). Meanwhile, the enhanced surface hydrophobicity resulted in surface B-enrichment in the Ni-B alloys. Since the aforementioned XPS spectra demonstrated that B donates partial electrons to Ni in the Ni-B alloy [41], the higher B-content in the Ni-B alloy made the metallic Ni more electron-enriched. On one hand, higher electron density in Ni active sites might facilitate the formation of H^- species [43], leading to higher TOF since the rate determining step was a nucleophilic attack of hydride ion on the nitrogen atom of the nitro group [44]. On the other hand, the electron-enrichment in Ni was also favorable for activating the adsorbed NO_2-group through a back electron-donation from $d_{x^2-y^2}$ orbital of Ni to $\pi^*_{N=O}$ anti-bonding orbital of N=O group, which could further enhance the TOF [45].
2. Although the weaker hydrophobicity, the Ni-B/NH_2-SBA-15 catalysts were more active than the Ni-B/CH_3-SBA-15 with the same content of organic groups. This could be mainly attributed to

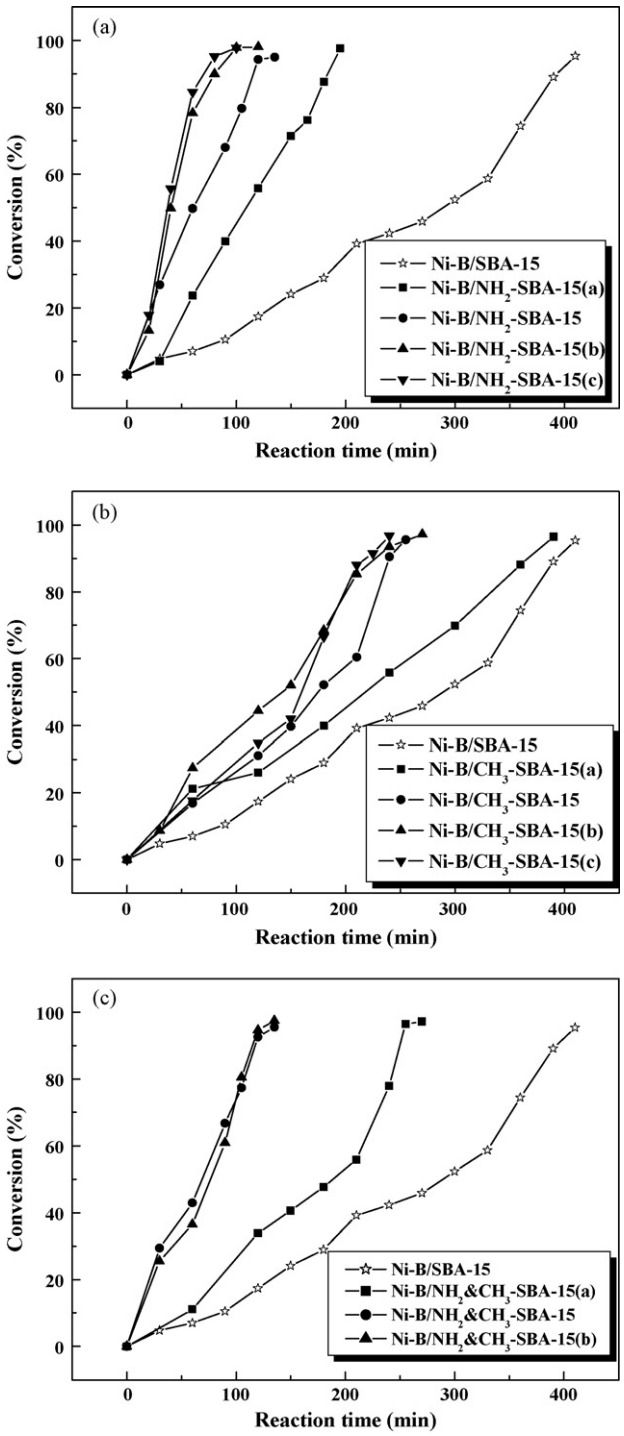

Fig. 10. Time–conversion curves of *p*-CNB hydrogenation over Ni-B/SBA-15 and Ni-B catalysts supported on (a) NH_2-SBA-15(*x*), (b) CH_3-SBA-15(*x*), and (c) NH_2&CH_3-SBA-15(*x*). Reaction conditions are listed in Table 2.

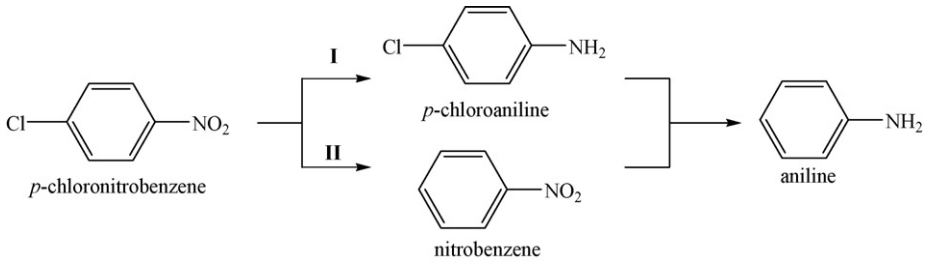

Scheme 1. A plausible pathway of *p*-CNB hydrogenation.

the smooth reduction of Ni^{2+} by BH_4^- owing to the coordination of Ni^{2+} with NH_2-groups incorporated into the mesoporous channels of SBA-15, which could promote the dispersion of Ni-B nanoparticles and also enhance the B-content in the Ni-B alloy, leading to higher S_{Ni} and enhanced TOF.

3. Fig. 11 illustrated the dependence of *p*-CAN selectivity on *p*-CNB conversion during *p*-CNB hydrogenation over various supported Ni-B amorphous alloy catalysts, from which the maximum yields of *p*-CAN were calculated and listed in Table 2. For the Ni-B/CH_3-SBA-15 series catalysts, the selectivity increased gradually with the enhanced CH_3-content, which could be mainly attributed to the enhanced surface hydrophobicity and the increased B-content in the Ni-B alloys. According to Figs. 9 and 11, the main byproduct was AN and only trace of NB was detected throughout reaction process. Thus, the *p*-CNB hydrogenation mainly followed Route I in Scheme 1. The *p*-CNB was firstly adsorbed by the catalyst through the NO_2–Ni bonding. Then, the adsorbed NO_2-group was hydrogenated into NH_2-group, corresponding to the formation of the target product *p*-CAN. The further hydrogenation induced the dechlorination of *p*-CAN, leading to the formation of AN byproduct [21]:

$$p\text{-CAN} + H_2 \rightarrow \text{AN} + \text{HCl} \quad (1)$$

Since the NH_2-group was more hydrophilic than the NO_2-group, the enhanced surface hydrophobicity may facilitate the desorption of *p*-CAN molecules from the catalyst and therefore, suppressed its subsequent dechlorination [22]. Besides, the higher B-content in the Ni-B alloys could enhance the electron

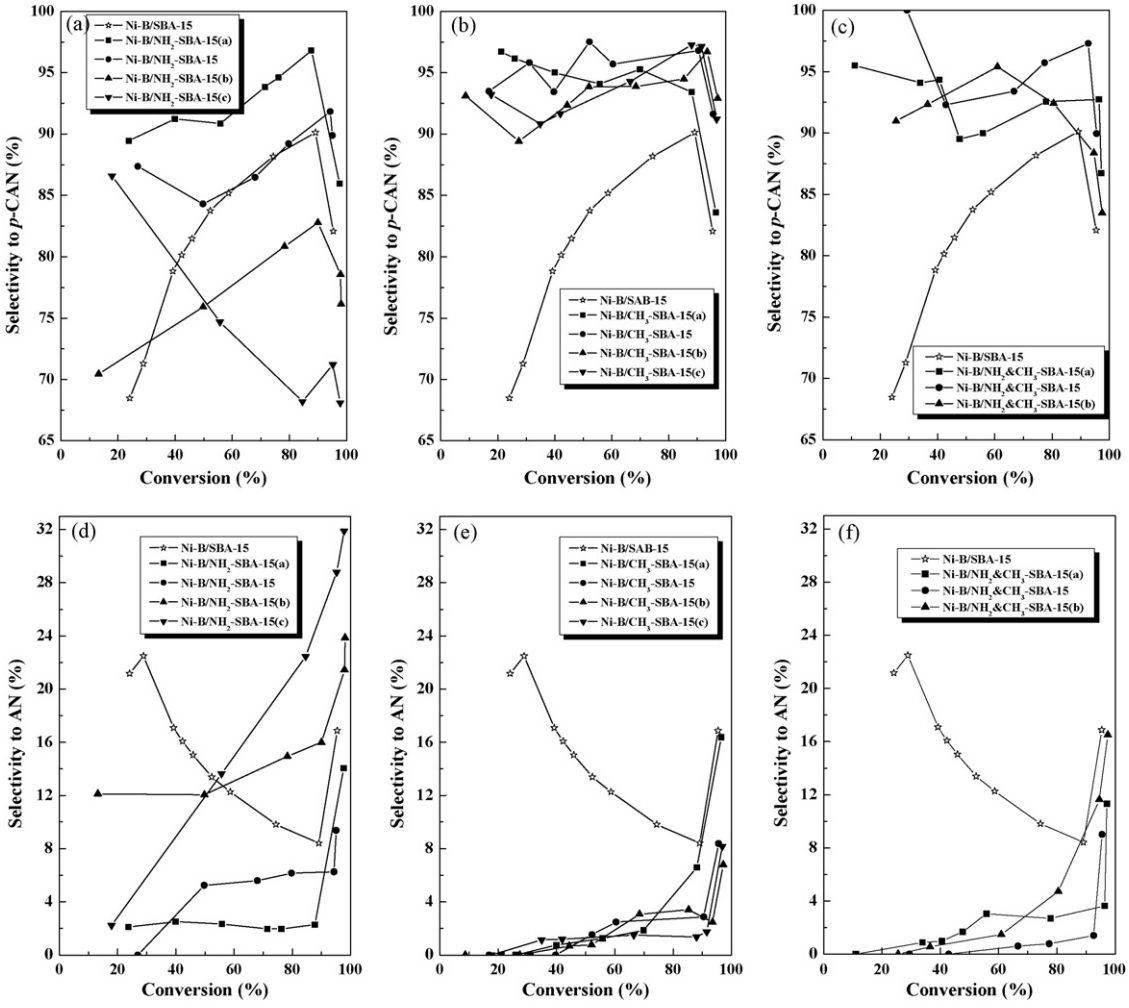

Fig. 11. Dependency of selectivity to (a) (b) (c) *p*-CAN, and (d) (e) (f) AN on conversion during *p*-CNB hydrogenation over all supported Ni-B amorphous alloy catalysts. Reaction conditions are listed in Table 2.

density of metallic Ni, taking into account that the B donated electrons to Ni in the Ni-B alloy, which facilitated the formation of H^- species [43] and also promoted the activation of NO_2-groups [45], leading to the higher selectivity to *p*-CAN. For the Ni-B/NH_2-SBA-15 series catalysts, the selectivity toward *p*-CAN first increased and then decreased with the enhanced NH_2-content. Similarly, the increase of the selectivity could be attributed to the enhanced surface hydrophobicity and the increased B-content in the Ni-B alloys owing to NH_2-functionalization of the support. At very high NH_2-content, the selectivity to *p*-CAN decreased due to the rapid increase of AN byproduct. A possible reason was the enhanced surface basicity, which promoted reaction (1) to produce AN byproduct, leading to the decrease in selectivity to *p*-CAN.

4. According to the above discussions, NH_2-functionalization could greatly promote the activity but its promotion on the selectivity to *p*-CAN was quite limited. The high NH_2-content was even harmful to the selectivity towards *p*-CAN. In contrast, CH_3-functionalization could greatly enhance the selectivity to *p*-CAN, but its promotion on the activity was quite limited. Ni-B/NH_2&CH_3-SBA-15 was superior to either Ni-B/NH_2-SBA-15 or Ni-B/CH_3-SBA-15 owing to the synergetic promoting effects from both the NH_2- and the CH_3-functionalizations.

4. Conclusions

This work developed a facile way to prepare SBA-15 type mesoporous silica co-functionalized with aminopropyl and methyl groups which was used as a support for depositing Ni-B amorphous alloy nanoparticles. During liquid-phase *p*-CNB hydrogenation to *p*-CAN, the as-prepared Ni-B/NH_2&CH_3-SBA-15 exhibited higher activity and better selectivity than either Ni-B/SBA-15 or Ni-B/NH_2-SBA-15 and Ni-B/CH_3-SBA-15, obviously owing to the synergistic promotional effects of both the aminopropyl group and the methyl group. On one hand, the aminopropyl incorporated into the silica framework greatly enhanced the dispersion degree of Ni active sites via coordination with Ni^{2+} ions, leading to high hydrogenation activity. On the other hand, the methyl anchored on the support enhanced the surface hydrophobicity, which facilitated the desorption of *p*-CAN and thus inhibited its further dechlorination to byproduct aniline. Besides, the methyl functionalization also enhanced the B-content in Ni-B alloys and thus donated more electrons to metal Ni, making the nitro group in the *p*-CNB molecule easily activated for hydrogenation, which further promoted the selectivity to *p*-CAN. By using the co-functionalized silica supports, other powerful amorphous alloy catalysts could be designed, which offered more opportunities for their industrial applications.

Acknowledgments

This work is supported by SHNU Leading Academic Discipline Project (DZL807), the National Natural Science Foundation of China (20603023), the 863 Project (2007AA03Z339), the Preliminary 973 Project (2005CCA01100), and Shanghai Government (09YZ158, S30406, 0852nm01000, 07dz22303).

References

[1] K. Klement, R.H. Willens, P. Duwez, Nature 187 (1960) 869.
[2] A. Molnar, G.V. Smith, M. Bartok, Adv. Catal. 36 (1989) 329.
[3] A. Baiker, Faraday Discuss. Chem. Soc. 87 (1989) 239.
[4] S. Yoshida, H. Yamashita, T. Funabiki, T. Yonezawa, J. Chem. Soc., Faraday Trans. 1 (80) (1984) 1435.
[5] Y. Chen, Catal. Today 44 (1998) 3.
[6] J.F. Deng, H.X. Li, W.J. Wang, Catal. Today 51 (1999) 113.
[7] H. Li, H.X. Li, W.L. Dai, J.F. Deng, Appl. Catal. A 207 (2001) 151.
[8] S.T. Wong, J.F. Lee, J.M. Chen, C.Y. Mou, J. Mol. Catal. A 165 (2001) 159.
[9] X. Chen, S. Wang, J. Zhuang, M. Qiao, K. Fan, H. He, J. Catal. 227 (2004) 419.
[10] A. Taguchi, F. Schüth, Micropor. Mesopor. Mater. 77 (2005) 1.
[11] K. Yamamoto, Y. Sunagawa, H. Takahashi, A. Muramatsu, Chem. Commun. (2005) 348.
[12] S. Inagaki, S. Guan, Y. Fukushima, T. Ohsuna, O. Terasaki, J. Am. Chem. Soc. 121 (1999) 9611.
[13] B.J. Melde, B.T. Hollande, C.F. Blanford, A. Stein, Chem. Mater. 11 (1999) 3302.
[14] T. Asefa, M.J. MacLachlan, N. Coombs, G.A. Ozin, Nature 402 (1999) 867.
[15] A.P. Wight, M.E. Davis, Chem. Rev. 102 (2002) 3589.
[16] F. Hoffmann, M. Cornelius, J. Morell, M. Fröba, Angew. Chem., Int. Ed. 45 (2006) 3216.
[17] N.T.S. Phan, C.S. Gill, J.V. Nguyen, Z.J. Zhang, C.W. Jones, Angew. Chem., Int. Ed. 45 (2006) 2209.
[18] E.L. Margelefsky, R.K. Zeidan, V. Dufaud, M.E. Davis, J. Am. Chem. Soc. 129 (2007) 13691.
[19] E.L. Margelefsky, A. Bendjériou, R.K. Zeidan, V. Dufaud, M.E. Davis, J. Am. Chem. Soc. 130 (2008) 13442.
[20] J.A. Melero, R. Van Grieken, G. Morales, Chem. Rev. 106 (2006) 3790.
[21] E. Thomas, J. Nickson, J. Org. Chem. 51 (1986) 3903.
[22] V. Kratky, M. Kralik, M. Mecarova, M. Stolcova, L. Zalibera, M. Hronec, Appl. Catal. A 235 (2002) 225.
[23] H. Li, J. Zhang, H.X. Li, Catal. Commun. 8 (2007) 2212.
[24] H. Li, Q.F. Zhao, H.X. Li, J. Mol. Catal. A 285 (2008) 29.
[25] H. Li, H. Lin, S.H. Xie, W.L. Dai, M.H. Qiao, Y.F. Lu, H.X. Li, Chem. Mater. 20 (2008) 3936.
[26] D. Zhao, J. Feng, Q. Huo, N. Melosh, G.H. Fredrickson, B.F. Chmelka, G.D. Stucky, Science 279 (1998) 548.
[27] Y. Wan, F. Zhang, Y.F. Lu, H.X. Li, J. Mol. Catal. A 267 (2006) 165.
[28] J.J.F. Scholten, A.P. Pijers, A.M.L. Hustings, Catal. Rev. Sci. Eng. 27 (1985) 151.
[29] L. Salvati, L.E. Makovsky, J.M. Stencel, F.R. Brown, D.M. Hercules, J. Phys. Chem. 85 (1981) 3700.
[30] H. Li, H.X. Li, W.L. Dai, W.J. Wang, Z.G. Fang, J.F. Deng, Appl. Surf. Sci. 152 (1999) 25.
[31] R.M. Rioux, H. Song, J.D. Hoefelmeyer, G.A. Somorjai, J. Phys. Chem. B 109 (2005) 2192.
[32] A. Yokoyama, H. Komiyama, H. Inoue, T. Masumoto, H.M. Kimura, J. Catal. 68 (1981) 355.
[33] D. Pérez-Quintanilla, I. Del Hierro, M. Fajardo, I. Sierra, Micropor. Mesopor. Mater. 89 (2006) 58.
[34] A.S. Maria Chong, X.S. Zhao, J. Phys. Chem. B 107 (2003) 12650.
[35] L.D. White, C.P. Tripp, Colloid Interface Sci. 232 (2000) 400.
[36] D.J. Macquarrie, D.B. Jackson, J.E.G. Mdoe, J.H. Clark, New J. Chem. 23 (1999) 539.
[37] K.S. Martens, J.A. Parton, R. Vercruysse, K. Jacobs, P.A. Maier, Catal. Lett. 38 (1996) 209.
[38] A. Fukuoka, Y. Sakamoto, S. Guan, S. Inagaki, N. Sugimoto, Y. Fukushima, K. Hirahara, S. Iijima, M. Ichikawa, J. Am. Chem. Soc. 123 (2001) 3373.
[39] X. Wang, K.S.K. Lin, J.C.C. Chan, S. Chen, J. Phys. Chem. B 109 (2005) 763.
[40] X.S. Zhao, G.Q. Lu, A.K. Whittaker, G.J. Millar, H.Y. Zhu, J. Phys. Chem. B 101 (1997) 6525.
[41] H.X. Li, H. Li, W.L. Dai, M.H. Qiao, Appl. Catal. A 238 (2003) 119.
[42] H.X. Li, H. Li, J. Zhang, W.L. Dai, M.H. Qiao, J. Catal. 246 (2007) 301.
[43] H. Noller, W.M. Lin, J. Catal. 85 (1984) 25.
[44] P. Lu, N. Toshima, Bull. Soc. Jpn. 73 (2000) 751.
[45] G.D. Yadav, M.R. Kharkara, Appl. Catal. A 126 (1995) 115.